Journal of Geodesy (2025) 99:25
https://doi.org/10.1007/s00190-025-01944-8

ORIGINAL ARTICLE

Translated spherical harmonics for semi-global gravitational field modeling: examples for Martian moon Phobos and asteroid 433 Eros

Xuanyu Hu[1]

Received: 22 March 2024 / Accepted: 7 February 2025

Abstract

The gravitational field of a planetary body is most often modeled by an exterior spherical harmonic series, which is uniformly convergent outside the smallest mass-enclosing sphere centered at the origin of the coordinate system, known as the Brillouin sphere. The model can become unstable inside the spherical boundary. Rarely deliberated or emphasized is an obvious fact that the radius of the Brillouin sphere, which is the maximum radius coordinate of the body, changes with the origin. The sphere can thus be adjusted to fit a certain convex portion of irregular body shape via an appropriate coordinate translation, thereby maximizing the region of model stability above the body. We demonstrate that it is, while perhaps counterintuitive, rational to displace the coordinate origin from the center of figure, or even off the body entirely. We review concisely the theory and a method of spherical harmonic translation. We consider some textbook examples that illuminate the physical meaning and the practical advantage of the transformation, the discussion of which, as it turns out, is not so easily encountered. We provide seminormalized as well as fully normalized version of the algorithms, which are compact and easy to work with for low-degree applications. At little cost, the proposed approach enables the spherical harmonics to be comparable with the far more complicated ellipsoidal harmonics in performance in the case of two small objects, Phobos and 433 Eros.

Keywords Spherical harmonics · Coordinate system translation · Gravitational field

1 Introduction

Spherical harmonics (SHs) form a well-known solution to the Laplace's equation in the spherical coordinate system, and are most commonly used for gravity modeling of the Earth and extraterrestrial bodies. The gravitational potential is often expressed as a truncated series (Heiskanen and Moritz 1967),

$$V = \frac{GM}{R} \sum_{n=0}^{n_{\max}} \sum_{m=0}^{n} \left(\frac{R}{r}\right)^{n+1} \bar{P}_{nm}(\sin\varphi) \left(\bar{C}_{nm}\cos m\lambda + \bar{S}_{nm}\sin m\lambda\right), \tag{1}$$

where r, λ, and φ are the spherical coordinates of radius, longitude, and latitude, respectively, of the field point. GM is the gravitational parameter. R is a reference radius. $\bar{P}_{nm}$ are the normalized associated Legendre polynomials (ALPs) of degree n and order m. The normalized field coefficients, $\bar{C}_{nm}$, $\bar{S}_{nm}$, measure the phases and amplitudes of the field variations at corresponding wavelengths. They are related to the body's mass density moments:

$$\begin{bmatrix} \bar{C}_{nm} \\ \bar{S}_{nm} \end{bmatrix} = \frac{1}{(2n+1)MR^n} \int r^n \bar{P}_{nm}(\sin\varphi) \begin{bmatrix} \cos m\lambda \\ \sin m\lambda \end{bmatrix} \mathrm{d}M, \tag{2}$$

where the integration is over volume occupied by the body mass. The mass distribution is referred to a uniform sphere (or concentric shells), the nonzero-degree coefficients measure "nonsphericity," e.g., center-of-mass offset, oblateness, etc., of the body.

Evaluation in spherical coordinates is intuitive and efficient, making the model suited for analyzing the dynamics of field objects, such as spacecraft motion often referred to a (nonrotating) celestial frame (Brouwer and Clemence 1961; Scheeres 2012). By means of trigonometry the nonspherical potential can be converted into orbital elements and the body's angle of rotation. The perturbed motion is derived in

---

✉ Xuanyu Hu
xuanyuhu@gmail.com

[1] Institute of Space Technology & Space Applications,
University of the Bundeswehr Munich,
Werner-Heisenberg-Weg 39, 85577 Neubiberg, Germany

terms of time-varying elements directly, where the signatures of model coefficients can be distinguished (Kaula 1966). The coefficients are estimated in the orbit determination from observations of perturbed spacecraft motion (Montenbruck and Gill 2000). The SH model has been the standard issue in gravity field recovery campaigns for large and small planetary bodies alike.

Which is not to say the SHs always provide an optimal solution. Depending on the body shape and the desired model resolution, a SH series may be neither stable nor efficient. With each term yielding a global contribution, cancelation of model signals occurs at all resolutions and all locations (Beylkin and Cramer 2002). It becomes particularly undesirable at small wavelengths, or local scales, where unnecessary nullification increases computational cost. Regional, multiresolutional approaches have been proposed as a more efficient alternative (Freeden 1984; Vermeer 1995; Kusche et al. 1998; Schmidt et al. 2007; Klees et al. 2008; Jones et al. 2011). The instability lies with the spherical reference. The validity of the series is unconditional outside a limiting sphere that encloses the body mass but generally unsupported otherwise. Evaluation near a nonspherical shape, e.g., over flattened and concave surface areas, below the sphere risks the model to often unpredictable errors. This issue is briefly reviewed below.

1.1 Convergence of SH series

The series in (1) is, as $n_{\max} \to \infty$, uniformly convergent if $r > \underline{r}_{\max}$, where $\underline{r}_{\max}$ is the maximum radius of body mass. The condition is derived directly from the expansion of the reciprocal distance, or point-mass potential (Hobson 1931, see the example in sect. 2.1). The Brillouin sphere is defined as centered at the coordinate origin and with radius $\underline{r}_{\max}$, touching the outermost point of the body (Fig. 1). The behavior when $r < \underline{r}_{\max}$ is complicated and depends on the body's mass distribution, i.e., $\bar{C}_{nm}, \bar{S}_{nm}$. Convergence within the Brillouin sphere is possible for certain distributions (Moritz 1980). An extreme example is the potential of a homogeneous sphere, equivalent to that of a point mass. When the coordinate origin is located at the center, the potential is given by a single term, GM/r, which is valid everywhere except at the origin, i.e., into the body where Laplace's equation does not apply. The same singularity, when placed above the body (e.g., in a "grain of sand" or a "mountain" on top of the Earth), can upset the convergence thereat and underneath (Krarup 1969; Moritz 1980).

For generic shapes or landscapes encountered on planetary objects, many numerical investigations have invariably revealed divergent behavior of the SH model in the form of outstanding errors beyond a certain degree. The symptom is especially acute for small irregular-shaped objects, e.g., asteroids, natural satellites, on which a mountain can dominate the global figure. (See, e.g., Sjöberg 1980; Jekeli 1981, 1983; Werner and Scheeres 1996; Garmier and Barriot 2001; Hu and Jekeli 2015; Reimond and Baur 2016; Sebera et al. 2016; Hirt and Kuhn 2017; Bucha and Sansò 2021). Costin et al. (2022) presented a proof that the SH series is virtually always divergent inside the Brillouin sphere for a multi-peak planetary topography. The attenuation rate of the surface harmonics gave the same impression (Kholshevnikov 1977; Kholshevnikov and Shaidulin 2015).

Krarup (1969) leveraged Runge's theorem and proved the existence of a harmonic function whose domain extends down to a(n arbitrary) sphere fully inside the body (and thus includes the entire free space) and which approximates the true potential arbitrarily well. The series of that function is then without question convergent on and everywhere exterior to the body. However, this well-behaved, approximating series, which may or may not be easily found (since no specific recipe was given concerning its formulation; see, however, Klees et al. 2008; Bucha and Sansò 2021), is essentially different from, and says nothing about the divergent behavior of, the original SH series. That is, its existence should by no means be interpreted as an insurance of the model defined by Eqs. (1) and (2), with which this work is solely concerned.

1.2 Choice and translation of coordinate origin

The choice of the coordinate system origin rarely comes into question in practice. It seems only natural to set the origin close to the center of the body, e.g., of the (geometric) figure or its mass distribution. Doing so means that a model is referred formally to a sphere of radius R that approximates the body's global shape as closely as possible, and thus maximizes the model efficiency capturing the field variations around the body (even if a sphere may be inherently a poor fit).

In most cases, there is no need to emphasize (or harm to omit) that the Brillouin sphere is centered at the origin of the chosen coordinate system; (see Fig. 2-10, p. 60, Heiskanen and Moritz 1967, or Fig. 1 here). Because its radius is determined by $\underline{r}_{\max}$, the Brillouin sphere is not the smallest (i.e., minimum-volume) sphere enclosing the body (which would generally have multiple contact points on the surface), though the difference should be small for a nearly spherical shape. A translation of the origin will generally change $\underline{r}_{\max}$ and result in a different Brillouin sphere (Fig. 1B).

In the new coordinate system, say, of r', λ', φ', the model by Eq. (1) will comprise a different set of coefficients (Fig. 2). They refer to the same mass distribution and have the same physical meaning as defined by Eq. (2). However, the corresponding density moments are now measured in terms of r', λ', φ'. For example, the degree-1 coefficients, proportional to the Cartesian coordinates of the body's cen-

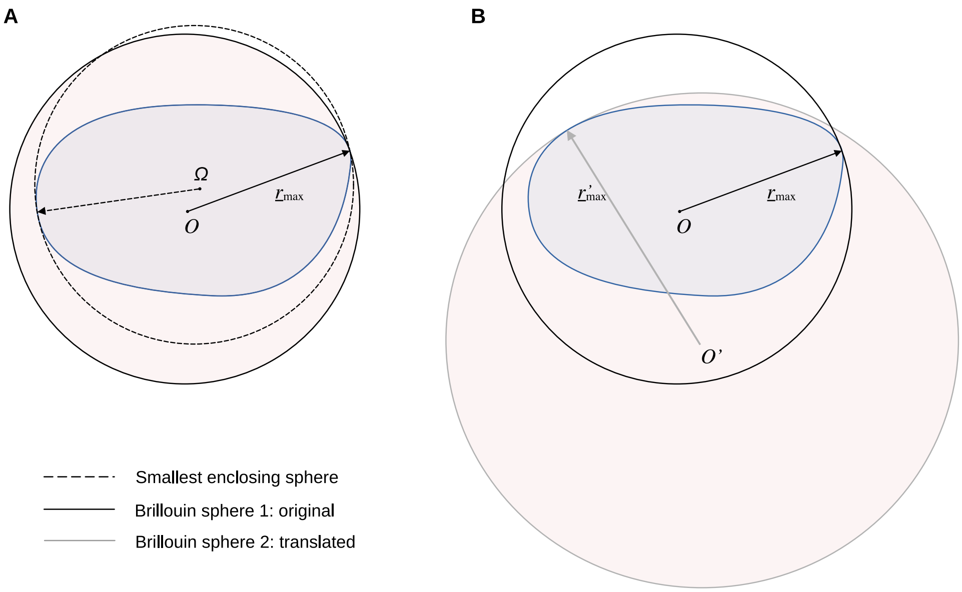

Fig. 1 Spherical boundaries. Brillouin sphere (centered at O) differs from the smallest enclosing sphere of body mass (centered at Ω) in origin as well as radius (**A**). Translation of origin from O to O' results in a different Brillouin sphere (**B**). The interior of the Brillouin sphere is light-shaded in red

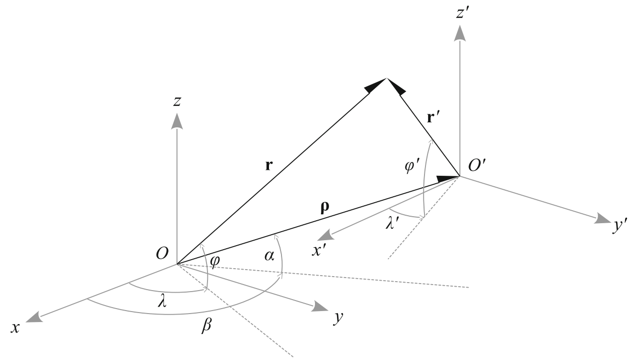

Fig. 2 Coordinate systems. $\boldsymbol{\rho}$ denotes translation vector measured in the old system. The position vectors of the field point are $\mathbf{r}(r, \varphi, \lambda)$ and $\mathbf{r}'(r', \varphi', \lambda')$ before and after translation, respectively. The translation is expressed by Eq. (11)

ter of mass, vanish if the origin coincides therewith after translation; similarly, the degree-2 coefficients of polar and equatorial "oblateness" are (re)measured about the new coordinate axes (see Sect. 3.3). We note that the tesseral coefficients, C_{21}, S_{21}, which measure the body's product of inertia, likewise change with the coordinate system.

1.3 Statement of problem

Crucially, the convergence space exterior to the Brillouin sphere changes after a coordinate translation. The effect may not be appreciable for a small translation, e.g., from the center of figure to the center of mass located often close by (or from Ω to O in Fig. 1A). A large translation, comparable to the body dimensions for instance, inevitably enlarges the Brillouin sphere whereby the *total* convergence space schrinks (Fig. 1B).

Totality has little meaning, however, if the model validity is overall doubtful, which is often the case around distinctly nonspherical objects (Fig. 1A). It may be sensible to sacrifice the globality of the model, if doing so can ensure its stability on a local scale. Specifically, the case of interest is a relatively flat, yet convex, surface portion (with respect to the global figure), which can be the polar region of an oblate body, or around the short axis of the elliptical equator. A translation can be designed to (just about) maximize the body radius by that over the area (as indicated by $\underline{r}'_{\text{max}}$ Fig. 1B). This way, the new Brillouin sphere closely fits the area in question while extending away from (all) the rest. The convergence space, while reduced overall, approaches the local surface to the extent possible.

Here we explore this simple strategy of trading model integrity for its local stability and demonstrate its effectiveness in improving the performance of the SH model around nonspherical bodies.

2 Effect of coordinate origin on model performance

We examine numerically three cases of series divergence: the potentials of a point mass, the Martian moon Phobos, and the asteroid 433 Eros. The point-mass case is also a well-known, theoretical example, by which the error signatures of the divergence are most easily identified. (Whereas, it seems that a specific numerical demonstration, however obvious and unnecessary one may assume, is not easily found in the literature.) Phobos and Eros both represent typical, nonspherical bodies. Phobos is however close to an ellipsoid and thus still "regular" in shape; Eros is highly irregular. The base simulations for Phobos and Eros are reproduced from results in several previous studies, Hu (2012), Hu and Jekeli (2015), and Hu (2016). We will examine the effect of a coordinate translation in each case.

2.1 Point mass

Let a point mass be located at the North Pole, $\underline{\mathbf{r}} = (0\ 0\ 1)^{\mathrm{T}}$. The series expansion of its potential is derived from that of the reciprocal distance:

$$\frac{1}{\ell} = \frac{1}{|\mathbf{r} - \underline{\mathbf{r}}|} = \sum_{n=0}^{\infty} r^{-n-1} \bar{C}_{n0} \bar{P}_n(\sin\varphi), \quad \bar{C}_{n0} = (2n+1)^{-1/2}. \tag{3}$$

As indicated in almost any textbook, the series is convergent everywhere $r > 1$, hence the designation exterior series. Less often explicated yet easily verifiable, e.g., via the nth-term test, is that the exterior series is divergent everywhere $r < 1$.

Because we deal with finite-resolution models in practice, it is the error behavior of a truncated series that is of interest. Figure 3 shows the difference of the series up to degree 5 and 15 from the true ℓ^{-1} in percentage within the y-plane. The regions within and outside the Brillouin sphere exhibit contrasting behaviors. Where the series is convergent, increasing the model resolution reduces errors. The errors of the two model resolutions are dominated by those of degrees 6 and 16, respectively, indicating they are residual, or due to series truncation, by character. The attenuation of errors with distance results from the fact that signals decrease in amplitude at all resolutions, in this case, at degrees 6 and 16.

Where $r < 1$, the errors are more significant and intensify with depth, e.g., reaching 100 % quickly below the Brillouin sphere. The pattern also differs in that the frequencies are visibly dominated by degrees 5 and 15, respectively, e.g., within the 100-% contours. This clearly indicates the errors are divergent in nature, as the omission errors would be only eminent beyond the model resolution. Another telltale sign is the intensification of errors with both resolution and depth, with the 100-% contours pushing toward the Brillouin sphere. The errors will still approach as the resolution increases further and fill the Brillouin sphere asymptotically.

Note that using Eq. (3) to evaluate a single point-mass potential would be incomprehensible in practice. The infinite series reduces to the $1/r$, if the coordinate origin is translated to coincide with the point mass.

2.2 Phobos

The Brillouin sphere of Phobos with respect to the same coordinate system for the shape model by Willner et al. (2014) is shown in Fig. 4A. The flattened figure leaves 56 % of the volume unoccupied, as the polar regions withdraw into the Brillouin sphere. The maximum depth in excess of 6 km occurs near the South Pole. Significant departure exists also around the equator with a secondary ellipticity and within the largest crater Stickney.

We assume Phobos has a uniform density of 1876 kg/m^3 (Andert et al. 2010). The gravitational field model of the body is obtained via a boundary value problem (Heiskanen and Moritz 1967),

$$\begin{bmatrix} \bar{C}_{nm} \\ \bar{S}_{nm} \end{bmatrix} = \frac{R}{4\pi GM} \int_0^{2\pi} \int_{-\pi/2}^{\pi/2} V(R, \varphi, \lambda) \bar{P}_{nm}(\sin\varphi) \begin{bmatrix} \cos m\lambda \\ \sin m\lambda \end{bmatrix} \cos\varphi \mathrm{d}\varphi\, \mathrm{d}\lambda, \tag{4}$$

where the potential V is evaluated on the Brillouin sphere using the method by Werner and Scheeres (1996). Numerical quadrature is based on a grid of 100×200 points in latitude and longitude, respectively. The same approach was adopted in Hu (2012) and Hu and Jekeli (2015), where the impact of the finite grid resolution on the derived coefficients as well as on the reconstructed potential was discussed in detail.

The evaluation error of the model is defined as the discrepancy from the truth in percentage:

$$\Delta V\ (\%) = \frac{\hat{V} - V}{V} \times 100\ \%, \tag{5}$$

where $\hat{V}$ is evaluated by the model. We note that V must also be erroneous compared with the "real" potential of the polyhedron, which is theoretically exact. The errors depend on the machine precision as well as algorithms of the numerical computation. However, because the field coefficients are directly evaluated from V, the imperfection of the latter does not affect the assessment of the SH model errors via Eq. (5).

Figure 4B and 4C show the errors of the models up to degree 5 and 20, respectively, in a plane containing the polar (z) axis and crossing Stickney. The errors display similar patterns to those in Fig. 3 but are smaller in magnitude, suggesting their behavior depends on the mass distribution. They are extensively reduced at degree 20, both outside and within a certain distance into the Brillouin sphere. In the immediate vicinity of the body, however, the errors become intensified at the higher-frequency similar to the divergence effect. The comparison is most evident on the body surface (panels D and E). The maximum errors, occurring in both cases at the poles, were enhanced from 5.2 % to 94 % at degree 20.

A sphere can be adjusted to fit the local surface curvature closely. This cannot be achieved by changing only the radius, and the center position must be treated as additional parameters. As an illustration, we devise a model for the northern half of Phobos by setting the origin of the coordinate system to (0.114, -1.16, -4.34) km in the original system. The position

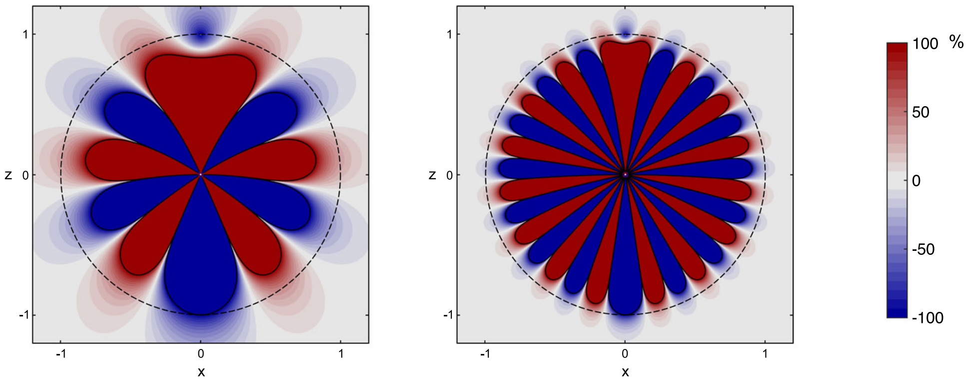

Fig. 3 Errors of Coulomb expansion modeled by SH series up to degree 5 (left panel) and degree 15. The solid black line contours the level of 100%. Larger errors are over-saturated

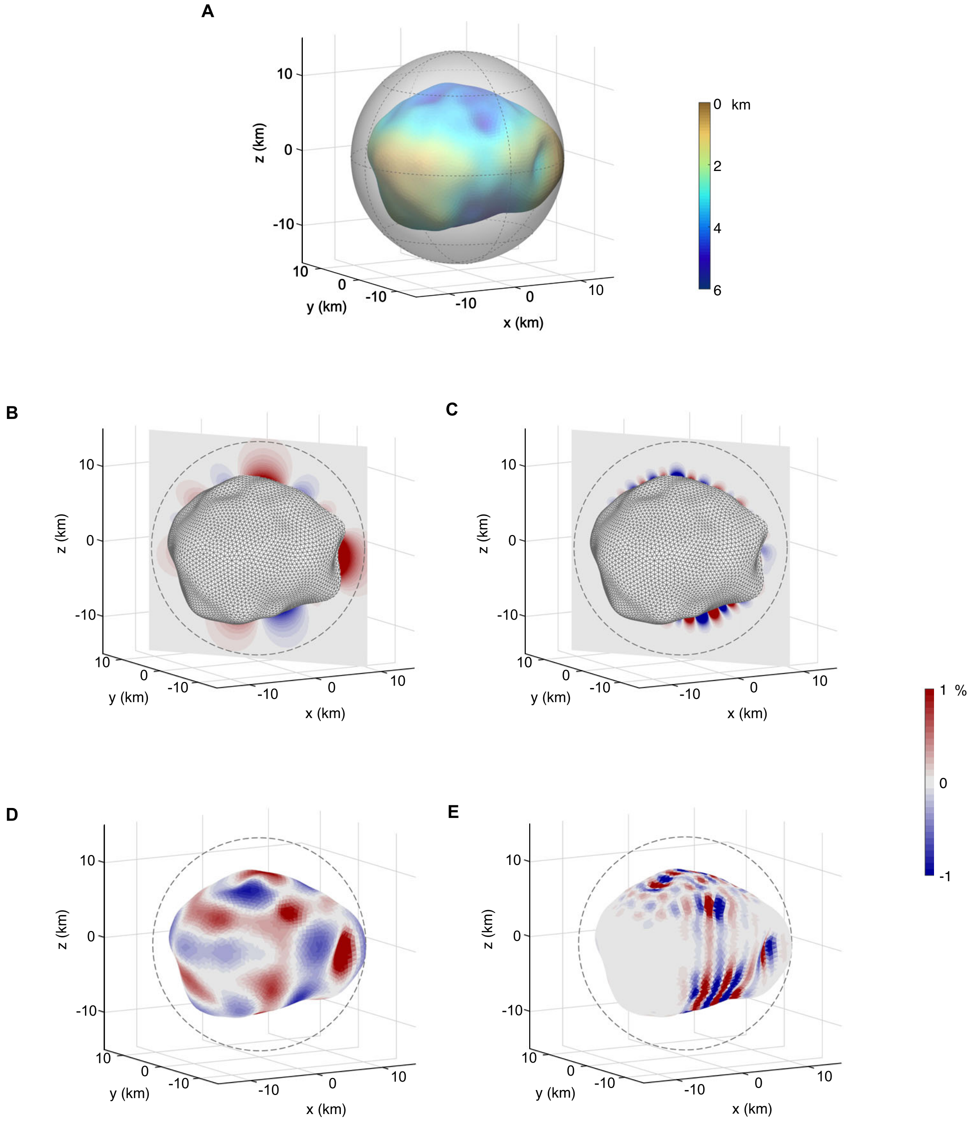

Fig. 4 SH model for Phobos. **A**. Depth of the body surface below the Brillouin sphere. **B**. Potential errors of the degree-5 model within a meridian plane passing Stickney. **C**. Errors of the degree-20 model in comparison. **D**. Errors of the degree-5 model on the body surface. **E**. Errors of the degree-20 model. Out-of-range errors are represented uniformly by the colors at the corresponding limits

Fig. 5 SH model for the northern half of Phobos. **A**. Depth of the body surface below the Brillouin sphere centered at (0.114, −1.16, −4.34) km. **B**. Potential errors of the degree-5 model within the meridian plane passing Stickney. **C**. Errors of the degree-20 model in comparison. **D**. Errors of the degree-5 model on the body surface. **E**. Errors of the degree-20 model

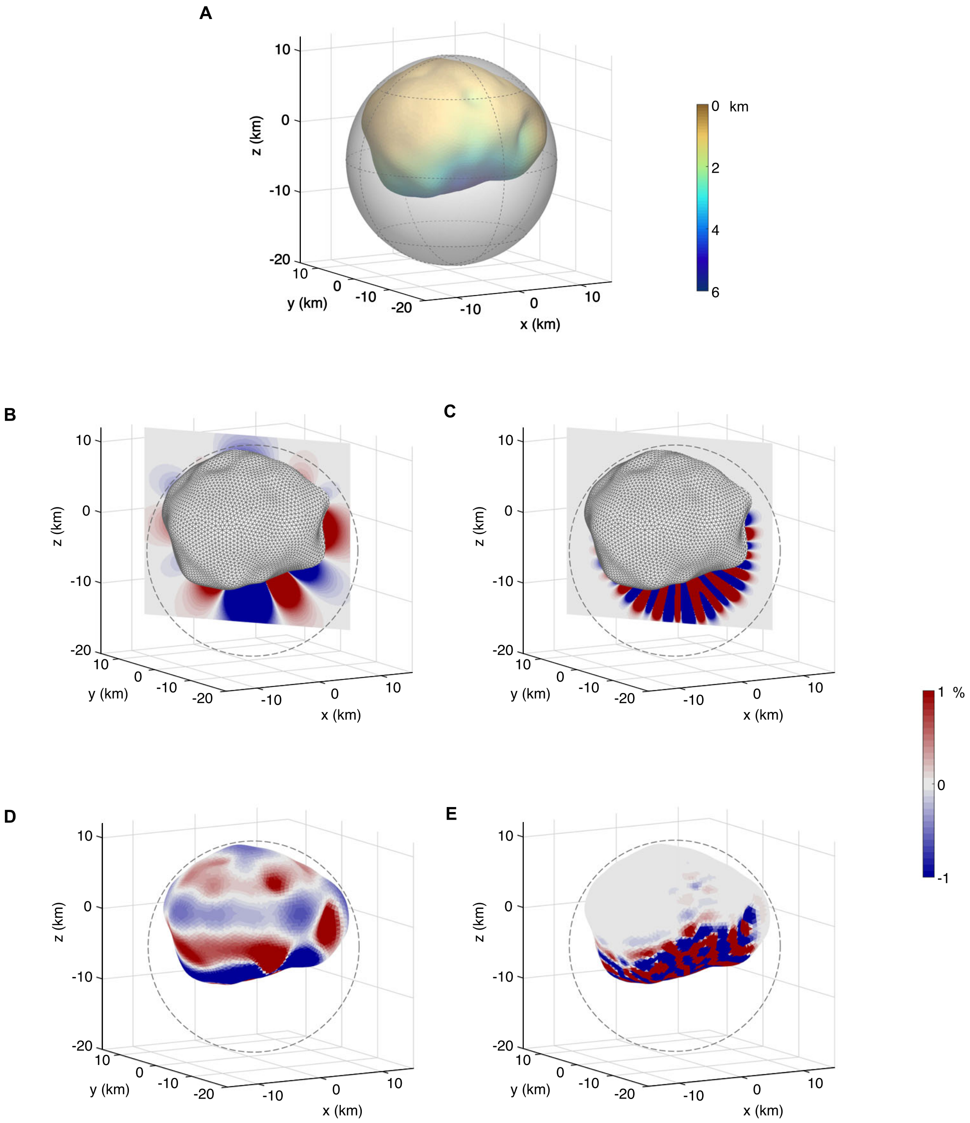

is found as the center of best-fitting sphere to the northern half of the shape model. The maximum body radius of 14.7 km measured therefrom defines a new Brillouin sphere, which covers snugly the northern half of Phobos but bulges away from the south (Fig. 5A).

The model, developed via (4) as before, shows the expected dichotomous behavior. The region above the south is more error-prone regardless of the model resolution (Fig. 5D,E). The errors are amplified closer to the body, i.e., clearly governed by the depth into the Brillouin sphere. Increasing the model resolution from degree 5 to 20 exacerbates the errors from an overall depth of 5 km. The deterioration is again most notable on the surface with errors exhibiting higher-frequency and stronger oscillations that no longer represent omission signals. The maximum errors increase from 800 % in the degree-5 model to 10^9 % at degree 20, neither value has any practical meaning.

In comparison, the model remains desirably valid over the north down to the body surface, evidenced by a significant error reduction as the model resolution increases. For instance, the errors of the model up to degree 20 are mostly contained within 1 % on the surface (with an indistinct error pattern in 5E), an order-of-magnitude decrease from those in the degree-5 model. Therefore, the displacement of the coordinate origin off the body center has yielded a more reliable model for the northern half of Phobos, at the expense of its applicability over the south.

2.3 Eros

The SH model exhibits only mild shortcomings for the overall convex Phobos, where the errors are comparable to the actual potential in magnitude. Eros presents a more emphatic case due to its elongated, partially bilobed shape. For example, the gravitational field of Phobos can be adequately modeled by the ellipsoidal harmonic series, which accommodates the triaxiality of the shape. However, the ellipsoidal model is far from robust near Eros, an issue that will be revisited later in this work.

Eros' gravitational field is simulated using the shape model of 10,000 facets by Thomas et al. (2002) and assuming again homogeneity with a bulk density of $2670\,\mathrm{kg/m^3}$ for the body (Miller et al. 2002). The Brillouin sphere has a radius of 17.7 km, with 89 % of its volume unoccupied (Fig. 6A). The waist formed by the depressions to both east and west is the deepest region on the body, with the entire western side ($y < 0$) sunken along a long, inward curve. The SH model in the original coordinate system is subject to crippling errors around the body, regarded (accentuated) here as over 100 % in magnitude, far more severe than those encountered on Phobos. Increasing the model resolution from degree 5 to 20 aggravates the errors, with the 100 % contours expanding visibly toward the Brillouin sphere (Fig. 6B,C). The model up to degree 5 incurs larger errors over 17 % of the surface area (D), compared with 64 % up to degree 20 (E). The maximum errors of 10^4 % and 10^{13} % at the respective resolutions can only be caused by series divergence.

Because the shape recedes on the western side, which cannot be closely fit inside any (exterior) Brillouin sphere, we attempt to improve the SH model over the north-eastern part that is predominantly convex notwithstanding a larger crater, Himeros (surrounding the positive y-axis) (Thomas et al. 2002). A translation of the origin to (-2, -11.5, -11.1) km results in a Brillouin sphere of 23.7-km radius that closely follows the overall convexity of the surface (Fig. 7A). As in the case of Phobos, the new model exhibits a controlled dichotomy, with errors effectively alleviated on the eastern side, even within Himeros, but intensified elsewhere (Fig. 7B,C). The errors amount to several percent on average on the body surface in the degree-5 model, with a maximum of 11.9 % at the bottom of the crater (Fig. 7D). They are reduced by one order of magnitude at degree 20, while the maximum decreases more modestly to 6 % alluding to the onset of the divergence effect that would intensify at higher resolution at the depth (7E).

2.4 Summary

In the theoretical case of a shapeless point mass, the translation of the coordinate system contracts the SH series to a single term of GM/r thereby minimizing the divergence region to a singularity. On the other hand, the gravitation of a finite, arbitrary shape, such as Phobos or Eros, generally has an infinite bandwidth (even if a SH model is always truncated). A translation of the origin can be devised to enhance the stability of the SH model over a certain, convex portion of the body. This is justifiable, when the original model is overall incapacitated near the irregular shape so that model degradation over other areas, however severe, causes no harm so long as it is not applied globally.

It is conceivable to derive a few "semi-global" SH models, each with their own origins and tailored for different regions on the object of interest, such that the combination provides global, reliable coverage of the entire shape (see Sect. 4).

3 Exterior SH series under coordinate translation

We consider a more practical scenario where a base SH model is available, e.g., determined from radio and optical tracking of spacecraft (Montenbruck and Gill 2000). The goal is then to derive a new, equivalent model after a coordinate system translation. The formulation of a boundary value problem, as demonstrated in the previous section, is possible but inconvenient. In particular, the boundary in this case should not be the new Brillouin sphere, on which the original model would be liable to divergence, but rather a (larger) concentric sphere enclosing the original Brillouin sphere. Alternatively, it is feasible to estimate in the least-squares sense a new model that conforms to the existing over their common, convergent space.

We adopt an analytic approach in this work. The transformation properties of the SHs under a coordinate system change have been well studied and documented for more than a century, though the rotation problem had received a bit more attention and seen applications in geomagnetism and quantum mechanics (Wigner 1959; Jeffreys 1965; Steinborn and Ruedenberg 1973; Rico et al. 2013) In the geophysical and geodetic literature, the coordinate translation was comprehensively treated by James (1969) and Aardoom (1969), the latter of which dealt specifically with the gravitational field of the Earth. Giacaglia (1980) showed how the SH transformation is useful in various classic problems in celestial mechanics and geodesy, e.g., expressing the disturbing function of satellite perturbation, the mutual potential of two bodies, etc., where multiple coordinate systems are involved. Referring to James (1969), Casotto (2000) presented a transformation formula for the field coefficients that conforms to Aardoom's.

We rewrite eq. (1) in the symmetric, complex, and for the time being, *unnormalized* form,

$$V = \frac{GM}{R}\sum_{n=0}^{\infty}\sum_{m=-n}^{n}\left(\frac{R}{r}\right)^{n+1} P_n^m(\sin\varphi)\exp(-\mathrm{i}m\lambda)(A_n^m+\mathrm{i}B_n^m). \tag{6}$$

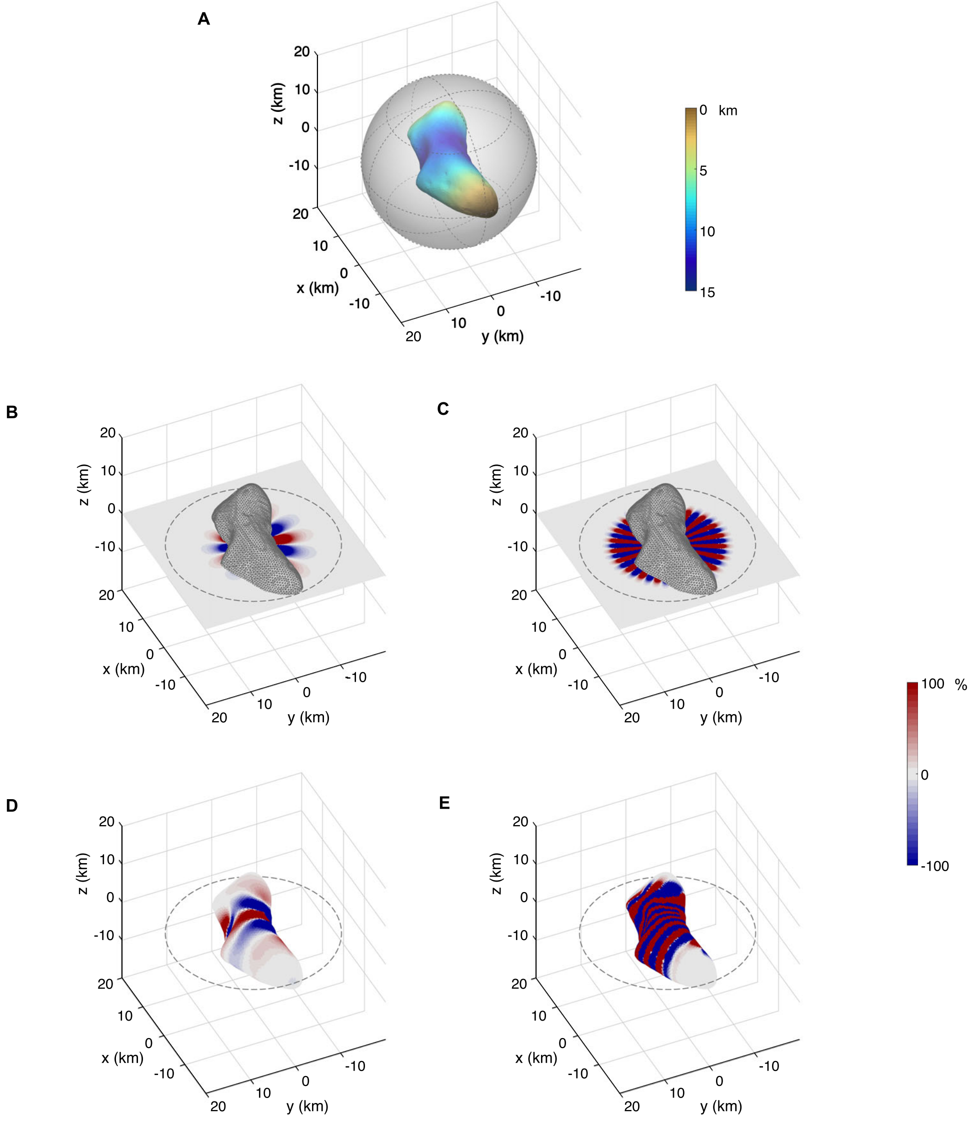

Fig. 6 SH model for Eros. **A**. Depth of the body surface below the Brillouin sphere. **B**. Potential errors of the degree-5 model within the equatorial plane. The dashed black line indicates the intersection of the Brillouin sphere. **C**. Errors of the degree-20 model in comparison. **D**. Errors of the degree-5 model on the body surface. **E**. Errors of the degree-20 model. Errors beyond 100 % in magnitude are represented uniformly by the colors at the corresponding limits

The ALPs are defined alternatively to those in (1) (Hobson 1931):

$$P_n^m = (-1)^m P_{nm}, \quad m \geq 0, \tag{7}$$

and have the following properties

$$P_n^{-m} = (-1)^m \frac{(n-m)!}{(n+m)!} P_n^m. \tag{8}$$

The complex coefficients are defined by (Aardoom 1969; Giacaglia 1980),

$$A_n^m + \mathrm{i}B_n^m = \frac{(n-m)!}{(n+m)!} \frac{1}{MR^n} \int_M r^n P_{nm}(\sin\varphi) \exp(\mathrm{i}m\lambda)\, \mathrm{d}M, \tag{9}$$

where the coordinates in the integrand refer to the body interior. Analogous to the ALPs, the following relation exists

$$A_n^{-m} + \mathrm{i}B_n^{-m} = (-1)^m \frac{(n+m)!}{(n-m)!} (A_n^m - \mathrm{i}B_n^m). \tag{10}$$

The conversion between $A_n^m + \mathrm{i}B_n^m$ and $\bar{C}_{nm}, \bar{S}_{nm}$ can be easily found but is of little use here. It will become evident, however, via an intermediate (seminormalized) expression (see Eq. 19).

3.1 Aardoom's transformation formula

To establish the transformation of the SH model under a translation, say

$$\mathbf{r}' = \mathbf{r} - \boldsymbol{\rho}, \quad \boldsymbol{\rho} = \rho\,(\cos\alpha\cos\beta \quad \cos\alpha\sin\beta \quad \sin\alpha)^{\mathrm{T}}, \tag{11}$$

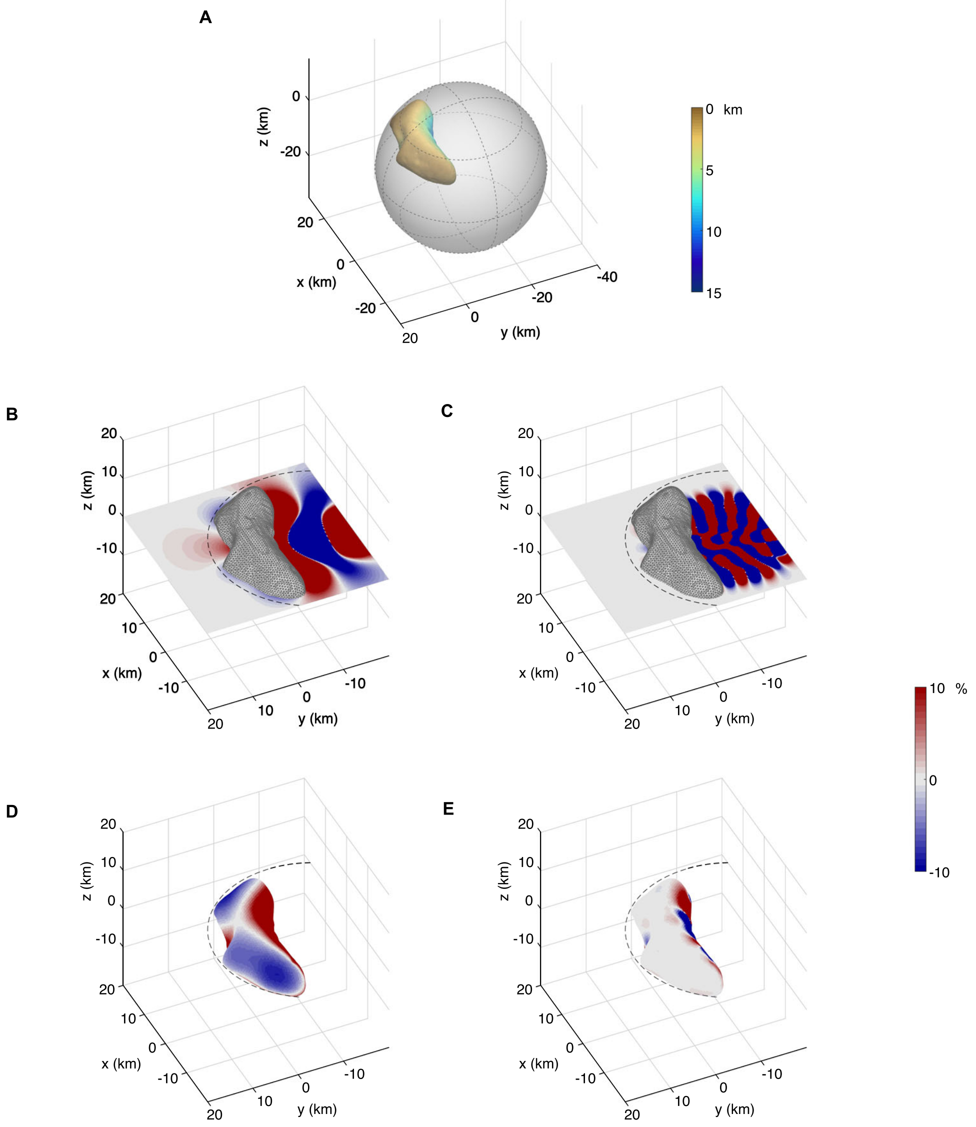

Fig. 7 SH model for the north-eastern side of Eros. **A**. Depth of the body surface below the Brillouin sphere centered at $(-2, -11.5, -11.1)$ km. **B**. Potential errors of the degree-5 model within the equatorial plane. The dashed black line indicates the intersection of the Brillouin sphere. **C**. Errors of the degree-20 model in comparison. **D**. Errors of the degree-5 model on the body surface. **E**. Errors of the degree-20 model. Note the reduced error range between -10 % and 10 % compared to that in Fig. 6

where $\boldsymbol{\rho}$ points from the current to the new origin (Fig. 2), it is necessary to find the expression of the solid SHs. Aardoom (1969) defined a complex vector $\mathbf{u}(t) = \left(1-t^2 \;\; \mathrm{i}(1+t^2) \;\; -2t\right)^{\mathrm{T}}$. It is easily found that $(\mathbf{u}\cdot\mathbf{r})^n = \left(x+\mathrm{i}y-t^2(x-\mathrm{i}y)-2tz\right)^n$ satisfies the Laplace's equation, irrespective of the free parameter t. Let $(\mathbf{u}\cdot\mathbf{r})^n$ take the form up to the power of t^{2n}

$$(\mathbf{u}\cdot\mathbf{r})^n = t^n \sum_{m=-n}^{n} H_n^m(\mathbf{r})\, t^m, \tag{12}$$

where H_n^m is a generating function of degree n in terms of r. It can be shown that $H_n^m(\mathbf{r})$ is a solid harmonic (Hobson 1931, p.97),

$$H_n^m(\mathbf{r}) = (-2)^n \frac{(-1)^m n!}{(n+m)!}\, r^n P_n^m(\sin\varphi)\exp(\mathrm{i}m\lambda). \tag{13}$$

$(\mathbf{u}\cdot\mathbf{r}')^n$ is given by the binomial expansion:

$$(\mathbf{u}\cdot\mathbf{r}')^n = \sum_{k=0}^{n} \binom{n}{k} (\mathbf{u}\cdot\mathbf{r})^{n-k} \left(\mathbf{u}\cdot(-\boldsymbol{\rho})\right)^k. \tag{14}$$

Substituting (12) and (13) into (14) and rearranging the indices of summation in accord with the power of the trailing t^m (the preceding t^n will be canceled out) on both sides of the equation leads to the transformation formula of the solid SH:

$$r'^n P_n^m(\sin\varphi')\exp(\mathrm{i}m\lambda') = \sum_{k=0}^{n}\sum_{j=j_{\min}}^{j_{\max}} (-1)^{n-k}\binom{n+m}{k+j} \rho^{n-k} P_{n-k}^{m-j}(\sin\alpha)\exp(\mathrm{i}(m-j)\beta)\, r^k P_k^j(\sin\varphi)\exp(\mathrm{i}j\lambda), \tag{15}$$

where $j_{\max} = \min(k, m+n-k)$ and $j_{\min} = \max(-k, m-n+k)$ consistent with $P_n^m = 0$ in case $|m| > n$.

The transformation of the coefficients proceeds with the integration over mass by (9) on both sides of (15), after cancelation of the factors, $(n+m)!$ and $(k+j)!$, yields eventually:

$$A_n'^m + \mathrm{i}B_n'^m = \sum_{k=0}^{n}\sum_{j=j_{\min}}^{j_{\max}} (-1)^{n-k}\frac{(n-m)!}{(n+m-k-j)!(k-j)!} \left(\frac{\rho}{R'}\right)^n \left(\frac{R}{\rho}\right)^k P_{n-k}^{m-j}(\sin\alpha) \exp(\mathrm{i}(m-j)\beta)\left(A_k^j + \mathrm{i}B_k^j\right). \tag{16}$$

The expression differs from Aardoom's only by R'^{-n} instead of R^{-n} in the radial function. The marginal difference arises when we accommodate $R' \neq R$.

3.2 Normalization

3.2.1 Semi-normalization

The real normalized coefficients, $\bar C_{nm}$, $\bar S_{nm}$, are most commonly used in practice. To make use of (16), one could de-normalize and convert them into complex coefficients, distinguishing between positive and negative m, before the transformation and subsequently convert and normalize the resulting ones (back) into $\bar C'_{nm}$, $\bar S'_{nm}$ (Casotto 2000). The procedure is entirely feasible but somewhat circuitous. We turn to the seminormalized version:

$$\tilde P_n^m = \sqrt{\frac{(n-m)!}{(n+m)!}}\,P_n^m, \quad \tilde A_n^m + \mathrm{i}\tilde B_n^m = \sqrt{\frac{(n+m)!}{(n-m)!}}\left(A_n^m + \mathrm{i}B_n^m\right), \tag{17}$$

which differs from the Schmidt seminormalization by a factor of $\sqrt{2}$ (Winch et al. 2005).

There are two *formal* reasons to resort to seminormalization. First, it suppresses the factorial ratio $\frac{(n-m)!}{(n+m)!}$ and its inverse in *both* the old and new models. Note that the mirroring of the ALPs and of the coefficients by (8) and (10), respectively, is compacted as,

$$\begin{bmatrix} \tilde P_n^{-m} \\ \tilde A_n^{-m} + \mathrm{i}\tilde B_n^{-m} \end{bmatrix} = (-1)^m \begin{bmatrix} \tilde P_n^{m} \\ \tilde A_n^{m} - \mathrm{i}\tilde B_n^{m} \end{bmatrix}. \tag{18}$$

Otherwise, many expressions used hereafter to interpret the transformations would be cluttered with the ratios wherever the ALPs or the complex coefficients appear (if not the transformation formulas themselves), not to mention that two sets of indices are involved and must be distinguished. The conversion from the normalized into the seminormalized coefficients is

$$\tilde A_n^m + \mathrm{i}\tilde B_n^m = (-1)^m\sqrt{\frac{2n+1}{2-\delta_{m0}}}\left(\bar C_{nm} + \mathrm{i}\bar S_{nm}\right), \quad m \geq 0. \tag{19}$$

Hence, the transformation formula (see Eq. 21) will be (almost) directly connected with the model by (1).

Second, thanks mostly to (18), seminormalization retains, or even improves, the symmetry of the complex formulas. The potential has the exact same form as (6). The decomposition formula involving negative-order harmonics is compacted to the extent possible:

$$\ell^{-1} = \sum_{n=0}^{\infty}\sum_{m=-n}^{n} \frac{r'^n}{r^{n+1}}\tilde P_n^m(\sin\varphi)\exp(-\mathrm{i}m\lambda)\,\tilde P_n^m(\sin\varphi')\exp(\mathrm{i}m\lambda'), \tag{20}$$

assuming $r' < r$.

In particular, it is not difficult to show from (16) that the transformation of the seminormalized coefficients exhibits symmetry:

$$\tilde A_n'^m + \mathrm{i}\tilde B_n'^m = \sum_{k=0}^{n}\sum_{j=j_{\min}}^{j_{\max}} (-1)^{n-k}\sqrt{\binom{n-m}{k-j}\binom{n+m}{k+j}} \left(\frac{\rho}{R'}\right)^n \left(\frac{R}{\rho}\right)^k \tilde P_{n-k}^{m-j}(\sin\alpha) \exp\left(\mathrm{i}(m-j)\beta\right)\left(\tilde A_k^j + \mathrm{i}\tilde B_k^j\right). \tag{21}$$

While this expression does not come with a computational advantage, neither is the cost notably higher than that of (16). In particular, the numerators of the binomial coefficients are falling factorials of $\min\left(k \pm j, n \pm m - (k \pm j)\right)$ terms. The true appeal is the ease to implement it with minimal coding effort.

3.2.2 Transformation of real, normalized coefficients

Should one prefer to work directly with the real coefficients $\bar C_{nm}$, $\bar S_{nm}$ and the ALPs $\bar P_{nm}$ instead of $\tilde P_n^m$, the seminormalized version (21) serves as a plain, intermediate expression toward a fully normalized formula. Still, it seems most straightforward to retain the negative indices of j, due to its asymmetry about zero, but work only with $\bar C_{k|j|}$, $\bar S_{k|j|}$ in the original series. Recalling from Eq. (18) the conjugation of $\tilde A_k^j + \mathrm{i}\tilde B_k^j$ for $j < 0$ and the preceding $(-1)^j$ for $j > 0$, the following expression can be obtained for $m \geq 0$:

$$\begin{Bmatrix} \bar C'_{nm} \\ \bar S'_{nm} \end{Bmatrix} = (-1)^m\sqrt{\frac{1}{2n+1}}\sum_{k=0}^{n}\sum_{j=j_{\min}}^{j_{\max}} \left(-\frac{\rho}{R'}\right)^n \left(-\frac{R}{\rho}\right)^k$$

$$\times\sqrt{\delta'\frac{2k+1}{2(n-k)+1}\binom{n-m}{k-j}\binom{n+m}{k+j}}$$
$$(-1)^{\max(0,m-j)}\,\bar{P}_{n-k\,|m-j|}(\sin\alpha)$$
$$(-1)^{\max(0,j)}\left[\bar{C}_{k|j|}\begin{Bmatrix}\cos(m-j)\beta\\ \sin(m-j)\beta\end{Bmatrix}\right.$$
$$\left.+\mathrm{sgn}(j)\,\bar{S}_{k|j|}\begin{Bmatrix}-\sin(m-j)\beta\\ \cos(m-j)\beta\end{Bmatrix}\right], \tag{22}$$

where

$$\delta'=\frac{2-\delta_{m0}}{(2-\delta_{mj})(2-\delta_{j0})}=\begin{cases}1, & \text{if } j=m,\ \text{or } j=0;\\ \frac{1}{4}, & \text{elseif } m=0;\\ \frac{1}{2}, & \text{else.}\end{cases} \tag{23}$$

3.3 Low-degree model demonstration

We consider a few theoretical examples demonstrating the behavior of the SH model under a coordinate translation effected by (22).

3.3.1 Point mass: transformation into finite-degree model

The potential of a point mass located at the North Pole, $\boldsymbol{\rho}=(0\;0\;1)^{\mathrm{T}}$, involves an infinite series of zonal SHs with $\bar{C}_{k0}=(2k+1)^{-1/2}$ (Eq. 3). As is theoretically known and illustrated in Fig. 3, the series diverges everywhere inside the unit sphere centered at the origin. Now, let the origin be relocated to $\boldsymbol{\rho}$. All ALPs other than $\bar{P}_{(n-k)0}(\sin\pi/2)=\big(2(n-k)+1\big)^{1/2}$ in (22) vanish. Assuming $R'=R=1$, the transformation becomes

$$\bar{C}'_{n0}=\sqrt{\frac{1}{2n+1}}\sum_{k=0}^{n}(-1)^{n-k}\binom{n}{k}=\delta_{n0} \tag{24}$$

The potential is given by $GM/\ell=GM/r'$, now rid of the artificial divergence region due to the displacement of the coordinate origin from the source.

3.3.2 Total mass, center of mass, and oblateness under translation

The transformation should not change the physical meaning of the coefficients regardless of the mass distribution. We seek no proof here – it is given by Eq. (15) relating the translated solid harmonics to those in the original coordinates, from which the coefficients are derived – and focus instead on the expressions of a few low-degree coefficients in validation of Eq. (22) applicable to the normalized models, which are most common in practice. Because the new coefficients are affected by the original up to the same degree, namely, $k\le n$, it is found immediately that $\bar{C}'_{00}=\bar{C}_{00}=1$, i.e., the body mass is invariant.

The transformation of the degree-1 coefficients is: .

$$\begin{Bmatrix}\bar{C}'_{10}\\ \bar{C}'_{11}\\ \bar{S}'_{11}\end{Bmatrix}=\frac{1}{\sqrt{3}R'}\left(-\frac{\rho}{\sqrt{3}}\begin{Bmatrix}\bar{P}_{10}(\sin\alpha)\\ \bar{P}_{11}(\sin\alpha)\cos\beta\\ \bar{P}_{11}(\sin\alpha)\sin\beta\end{Bmatrix}+\sqrt{3}R\begin{Bmatrix}\bar{C}_{10}\\ \bar{C}_{11}\\ \bar{S}_{11}\end{Bmatrix}\right). \tag{25}$$

Since $\bar{P}_{10}(\sin\alpha)=\sqrt{3}\sin\alpha$, $\bar{P}_{11}(\sin\alpha)=\sqrt{3}\cos\alpha$, the first terms in the parentheses are $-\rho_z$, $-\rho_x$, and $-\rho_y$, respectively, as in Eq. (11). The Cartesian coordinates of the body's center of mass, which were originally $\frac{1}{M}\int(x\;y\;z)^{\mathrm{T}}\mathrm{d}M=\sqrt{3}R(\bar{C}_{11}\;\bar{S}_{11}\;\bar{C}_{10})^{\mathrm{T}}$, are shifted by $-(\rho_x\;\rho_y\;\rho_z)^{\mathrm{T}}$ after model transformation.

The degree-2 zonal coefficient measures the polar oblateness of the mass distribution: .

$$\bar{C}_{20}=\frac{1}{5MR^2}\int r^2\bar{P}_{20}(\sin\varphi)\mathrm{d}M=\frac{1}{\sqrt{5}MR^2}\int z^2-\frac{x^2+y^2}{2}\mathrm{d}M, \tag{26}$$

and undergoes a transformation,

$$\bar{C}'_{20}=\frac{1}{\sqrt{5}R'^2}\left(\frac{\rho^2}{\sqrt{5}}\bar{P}_{20}(\sin\alpha)-\rho R\right.$$
$$\Big[2\bar{P}_{10}(\sin\alpha)\bar{C}_{10}-\bar{P}_{11}(\sin\alpha)\left(\bar{C}_{11}\cos\beta+\bar{S}_{11}\sin\beta\right)\Big]$$
$$\left.+R^2\sqrt{5}\bar{C}_{20}\right). \tag{27}$$

Incorporating (26) and $\rho^2\bar{P}_{20}(\sin\alpha)/\sqrt{5}=\rho_z^2-(\rho_x^2+\rho_y^2)/2$ into the right-hand side gives

$$\bar{C}'_{20}=\frac{1}{\sqrt{5}MR'^2}\int(z-\rho_z)^2-\frac{(x-\rho_x)^2+(y-\rho_y)^2}{2}\mathrm{d}M, \tag{28}$$

which differs from (26) merely by a translation and the reference scale.

At last, we consider the sectoral case of $r^2\bar{P}_{22}(\sin\varphi)\cos 2\lambda=\frac{\sqrt{15}}{2}(x^2-y^2)$,

$$\bar{C}'_{22}=\frac{1}{\sqrt{5}R'^2}\left\{\frac{\rho^2}{\sqrt{5}}\bar{P}_{22}(\sin\alpha)\cos 2\beta-R\rho\sqrt{3}\bar{P}_{11}(\sin\alpha)\right.$$
$$\left.\Big[\bar{C}_{11}\cos\beta-\bar{S}_{11}\sin\beta\Big]+R^2\sqrt{5}\bar{C}_{22}\right\}$$
$$=\frac{1}{5MR'^2}\frac{\sqrt{15}}{2}\int(x-\rho_x)^2-(y-\rho_y)^2\,\mathrm{d}M, \tag{29}$$

which measures the body's equatorial flattening with respect to the axis, $x=\rho_x$ and $y=\rho_y$.

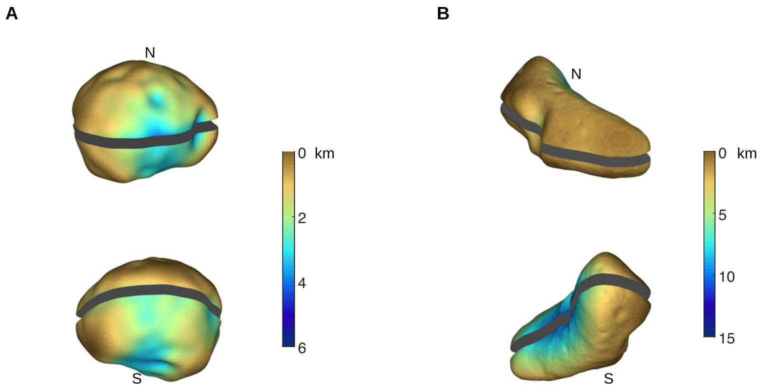

Fig. 8 Surface depths of the northern and southern halves of Phobos (**A**) and Eros (**B**), measured with respect to the respective Brillouin spheres after translation. The color scale is as in Figs. 4 and 6

The integrals for other coefficients can be obtained in the same way to verify the preservation of their physical meaning.

4 Translated models for Phobos and Eros

The feasibility of coordinate translation is a trade-off between the robustness and the coverage of the SH model (Sect. 2.2 and 2.3). It is most practical when the resultant models are not rendered too "local", so that a few, say, two or three, transformations suffice to ensure global coverage around the body. That is to say, it does not take too many (Brillouin) spherical segments to wrap around the body. This should be the case for many small bodies with convex shapes. Global concavities cannot be fit into an exterior sphere, however.

4.1 Phobos

In the case of moderately irregular Phobos, the translated model shown in Fig. 5D and E is mostly reliable over the north. To find a complementary hemispheric model, we determine the best-fitting sphere of the south, in this case originated at (0.21, -0.16, 2.86) km. The outermost point of the shape has a radius of 14.47 km. It should be pointed out this has not resulted in the smallest Brillouin sphere of the south, namely, one that would minimize locally the unoccupied volume of the spherical sector. The optimization, and any practical advantage thereof, is beyond the scope of this analysis. The depths of the body surface relative to the respective Brillouin spheres are shown in Fig. 8A. The root-mean-square of 3 km with respect to the original Brillouin sphere is nearly halved after translations, with the improvement more significant in the north (Table 1).

Table 1 Depth statistics on Phobos and Eros with respect to Brillouin spheres

Depth (km)		Phobos			Eros		
		North	South	Total	North	South	Total
original	Max	4.79	5.94		14.55	14.15	
	RMS	3.10	3.06	3.08	8.43	8.52	8.47
Translated	Max	3.94	3.58		10.19	9.94	
	RMS	1.27	1.94	1.64	3.83	3.71	3.77

We apply the formula of (22) for the model transformation up to degree 20. Figure 9A shows the errors of the transformed coefficients, $\bar{C}'_{nm}$, $\bar{S}'_{nm}$, evaluated as the discrepancy from those derived via the boundary value problem in percentage. The errors increase with degree and remain under 0.01 % up to degree 10. They are larger than the numerical uncertainty of the quadrature, which amounts to the maximum of about 10^{-7}.

We test two simple cases of model synthesis. First, only the translated models are used for the north and south, respectively, distinguished by the latitude, which we designate as the "translated" case (as in Table 2; Fig. 10). In the second, the translated models are used together with the original, where the model whose Brillouin sphere lies the closest to the field point is selected for evaluation, which is distinguished as the "translated+original" case.

We compare the results with those for the ellipsoidal harmonic models (Hu 2012; Hu and Jekeli 2015). Phobos has an exemplary triaxial figure, for which the ellipsoid serves as a natural geometric as well as geodetic reference (though less obvious, the same applies to the Earth, Hu 2017; Hu et al. 2023). The Brillouin ellipsoid has semiaxes of 14.5, 12.5, 10.5 km, with 71.3 % of the volume filled by the body compared to 44 % of the original Brillouin sphere (Fig. 11). The ellipsoidal harmonic model is overall stable on Phobos' surface. The potential error RMS of 0.15 % up to degree 20 is improved by more than an order of magnitude compared with that of the SH model (Table 2). Errors exceeding 1 % are localized along the equator, within the crater, and around the South Pole. The maximum of 2.2 % increased slightly by 0.6 % from that up to degree 10, which signals the gentle onset of divergence at degree 20.

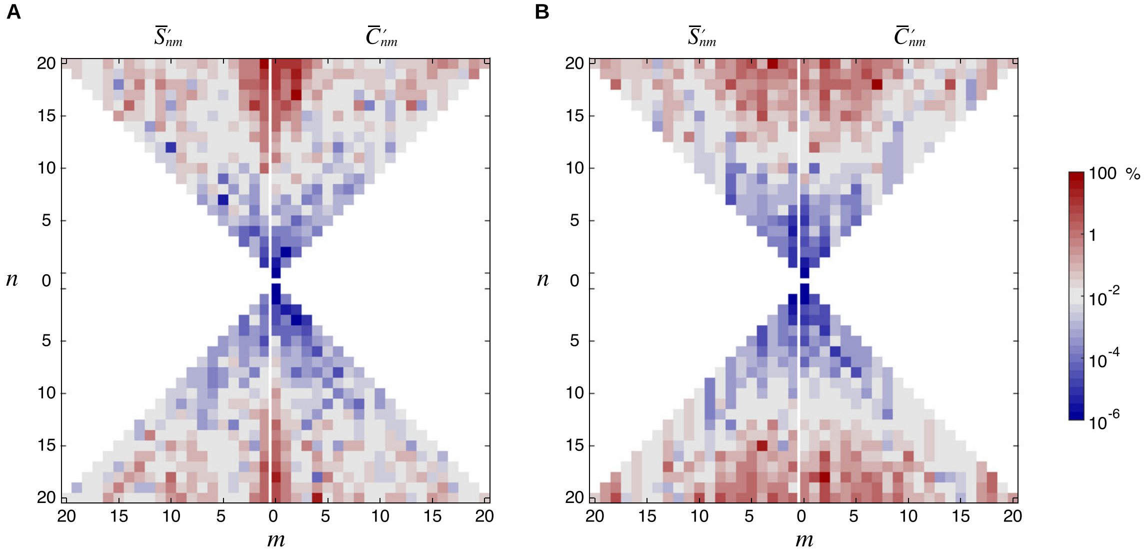

Fig. 9 Errors of translated coefficients for Phobos (**A**) and Eros (**B**). The upper (inverted) and lower triangles correspond to the models for the northern and southern hemispheres in each case. The white lines separate $\bar{C}_{nm}$ and $\bar{S}_{nm}$ (left)

Table 2 Error statistics of modeled potentials on Phobos and Eros up to degree 20

	ΔV		Phobos	Eros
Original	Max		93.8%	6.4×10^{13}%
	RMS		4.46%	2.45×10^{7}%
	Percentile ($\leq$)	10%	98.2	25.4
		1%	86.1	14.8
Translated	Max		8.62%	5.24×10^{3}%
	RMS		0.316%	352.8%
	Percentile ($\leq$)	10%	100	81.7
		1%	98.9	64.0
Translated + original	Max		5.44%	6.85×10^{3} %
	RMS		0.243%	767.8%
	Percentile ($\leq$)	10%	100	82.0
		1%	99.1	66.6
Ellipsoidal harmonic	Max		2.19%	2.21×10^{4}%
	RMS		0.152%	735.2%
	Percentile ($\leq$)	10%	100	83.6
		1%	99.5	70.4

The advantage over the translated SH model(s) is less remarkable. The maxima and the RMS are smaller but on the same order of 1 and 0.1 %, respectively. Both the SH and the EH can be evaluated (up to degree 20) over about 99 % of the surface area, if potential errors no greater than 1 % are regarded as tolerable. We note that the combination of the translated and the original models yields a modest improvement over the translation case, with a reduction of the maximum and RMS errors by 3 % and 0.07 %, respectively (Table 2). However, the ellipsoidal harmonics are intrinsically more efficient in the ellipsoidal spectrum and thus more accurate around a triaxial body up to the same degree (or requiring fewer terms to achieve the same accuracy) than the SHs (Garmier and Barriot 2001). Hence, the leading metrics of the ellipsoidal harmonic model hardly come as a surprise.

4.2 Eros

Similar to the approach for Phobos, we derive another translated SH model for the south-east of Eros, i.e., with the concave western side knowingly excluded from consideration. The translation vector is $(-1.8\ -11.6\ 11.9)^{\mathrm{T}}$ km and the Brillouin sphere has a radius of 24.1 km. The separation of the surface from the translated Brillouin spheres is notably

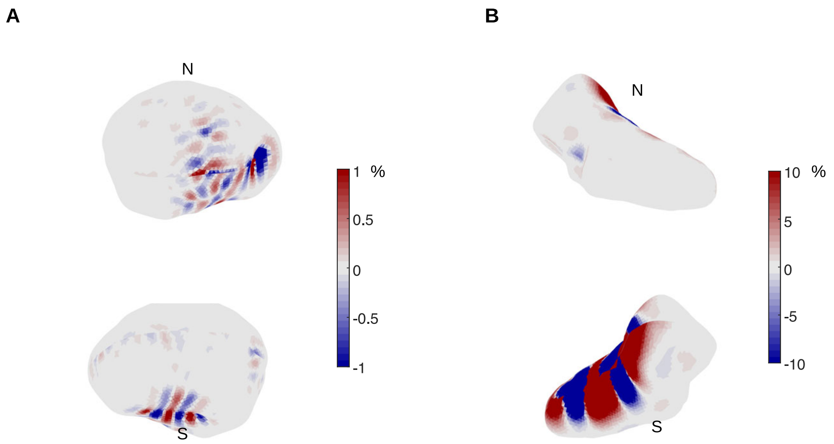

Fig. 10 Potential errors of combined translated SH models for Phobos (**A**) and Eros (**B**) up to degree 20

reduced compared with that from the original (Figs. 8B and 6A); the larger statistics compared with those for Phobos are due to the misfit of the western part (Table 1). The model extends the coverage of the one shown in Figure 7 to the entire convex eastern side of Eros.

Because of the asymmetry along two (equatorial) axes, Eros is a loose fit into the Brillouin ellipsoid with semiaxes of $23.1 \times 10.1 \times 7.6\ \mathrm{km}^3$, occupying 34.1 % of the volume. It is unsurprising then that ellipsoidal harmonics are barely suited for Eros and diverge near the nonellipsoidal body (Garmier et al. 2002). Nevertheless, they are not nearly as impaired as the original SH series (Fig. 6D,E), and can be applied over a much larger surface area (Table 2).

Where the ellipsoidal model is compromised, i.e., around much of the equatorial belt accounting for about 20 % of the surface, the translated SH models prove to be at least in part more resistant to failure. The errors are kept consistently below 10 % over the eastern side, for which the translations were purposed (Fig. 10B). We note again the marginal benefit of combining the translated and the original models, where the area fractions of errors below 10 % and 1 % expanded from 81.7 % to 82.0 % and from 64.0 % to 66.6 %, respectively. The EH and SH are both divergent on the concave western side, while the translated model is affected over a wider strip about the equator. The distributions of the errors at 10 % and 1 % are similar, with the ellipsoidal model being slightly more resilient (Table 2, Fig. 11).

5 Conclusion & discussion

It has been demonstrated that the translation of SH series can be used to improve the stability of the gravitational field model near a nonspherical body. The emphasis here is that a coordinate translation (nearly) always changes the Brillouin sphere, the consequence of which however can only be appreciated with a substantial shift. The approach trades the model integrity for its local performance, a worthy sacrifice in many cases (e.g., Eros). Global modeling is achieved by the combination of a few translated series. This flexibility allows the SHs to rival, if not outperform, the far more sophisticated EH model. While the SH translation has been well treated across disciplines, a search in the literature has not yielded any similar application (Fig. 11).

There could be two reasons for the singularity. First, insofar as gravitational field modeling is concerned, the translation problem has not been eagerly explored in a practical light. For instance, a field model is rarely transformed explicitly via (16); indeed, the closed-form formula was used by Aardoom (1969) to assess the impact of the center-of-mass offset on other (low-degree) coefficients, a question that later could be easily, if less deftly, solved via numerical methods. Second, effective alternatives to the SHs have been well studied in the literature, which could obviate the divergence issue of the global model (see, e.g., Klees et al. 2008). The present study shows on the other hand that, by relinquishing the global base, the translations can significantly alleviate the divergence effect.

Equations (21) and (22) are equivalent to the original formula by Aardoom and both can be easily implemented for the model translation; the latter is less compact in form but applies directly to the normalized gravity field models. They obviate the need for the two-way conversion between the real, normalized and the complex, unnormalized coefficients. We have not attended to the computational aspect, as the formulas suffice for the low-degree applications, e.g., up to degree 20 in the case of Phobos and Eros. The transformation of higher-degree models, should it be of interest, would require further investigation.

A practical question is how to optimize the synthesis of multiple models. This concerns maximizing the region of model convergence while invoking as few translations as possible. The model transition across boundaries also needs to be established. While this study could not touch these topics, the results here can still offer some insight. For instance, that the addition of the original to the translated models has not

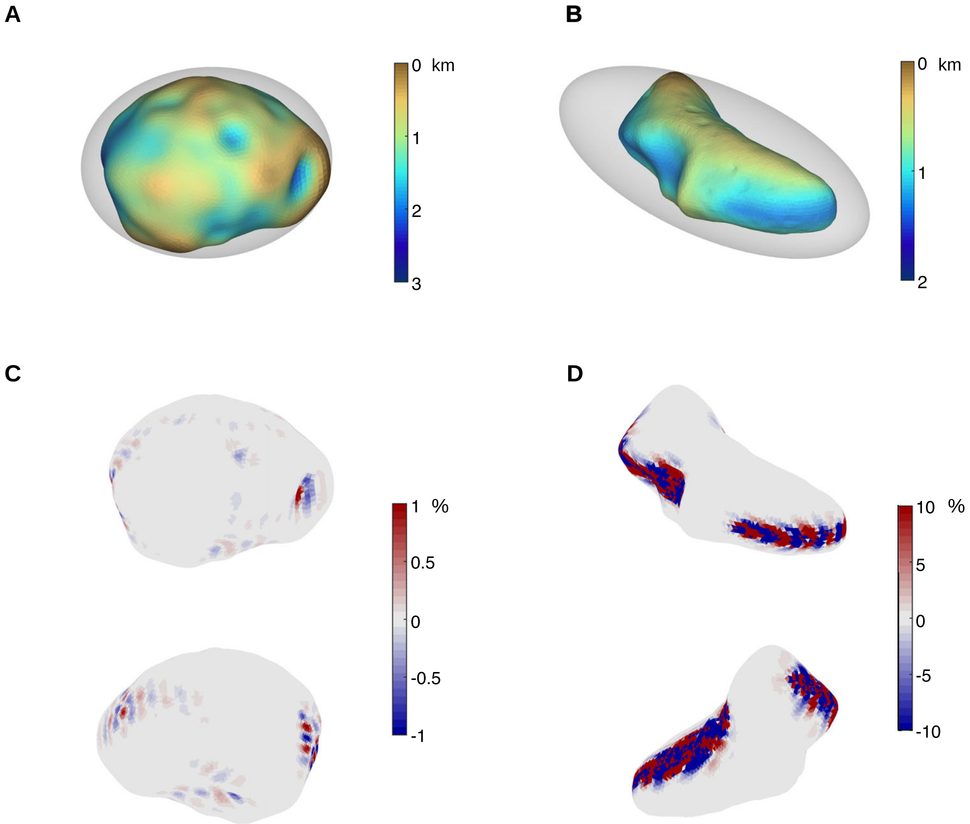

Fig. 11 EH models for Phobos and Eros. **A**. Surface depth of Phobos with respect to the Brillouin ellipsoid. **B**. Surface depth of Eros. **C**. Errors of modeled potential on Phobos up to degree 20. **D**. Errors on Eros up to model degree 20

proved beneficial (Table 2) suggests fine adjustment of the Brillouin spheres is not of critical importance to model performance. On the other hand, the most abrupt discontinuity of errors occurred along boundaries where both models are distinctly divergent (Fig. 10B), whereas the model transition at reasonable error levels is relatively smooth. This implies that the transition problem may only be relevant in the common divergence region of models.

The issue of (global) surface concavity, i.e., the western side of Eros, was unaddressed. The exterior series is inadequate in this case. An interior SH series should be employed instead, as discussed in Takahashi et al. (2013). That model is also applied locally, since the convergence space is the interior of the Brillouin sphere, which touches and excludes the body mass. It is worth pointing out that the exterior-interior SH transformation can also be accomplished by a coordinate translation; see James (1969).

Appendix A: Model uncertainty of Eros due to numerical quadrature

The field coefficients derived via numerical quadrature (Eq. 4) contain numerical errors. In this appendix we dissociate the overbar symbol from normalization, and C_{nm}, S_{nm} and P_{nm} are implicitly normalized quantities from now on. The integration can be approximated as

$$\begin{bmatrix} \hat{C}_{nm} \\ \hat{S}_{nm} \end{bmatrix} = \mathcal{I}_{nm}(V) = \frac{R}{4\pi GM} \times \sum_{i}^{200} \sum_{j}^{100} V(R, \varphi_j, \lambda_i) P_{nm}(\sin\varphi_j) \begin{bmatrix} \cos m\lambda_i \\ \sin m\lambda_i \end{bmatrix} \cos\varphi_j \Delta\varphi_j \, \Delta\lambda_i, \tag{A1}$$

where φ_j, λ_i are, respectively, the latitude and longitude of the grid point (i, j).

Rewrite the true potential as a partial sum in terms of degree p and order q,

$$V = \sum_{p=0}^{\infty} \sum_{q=0}^{p} V_{pq}, \tag{A2}$$

with $V_{pq} = (C_{pq} \cos q\lambda + S_{pq} \sin q\lambda) P_{pq}(\sin\varphi)$. Then, the model potential errors can be expressed as

$$\Delta V = \hat{V} - V = \Delta V^{(\mathrm{CF})} - \Delta V^{(\mathrm{OM})}, \tag{A3}$$

where $\Delta V^{(\mathrm{OM})}$ is the omission error, i.e., $\sum_{p=n_{\max}+1}^{\infty} \sum_{q=0}^{p} V_{pq}$. The other component, $\Delta V^{(\mathrm{CF})}$, is the contribution of

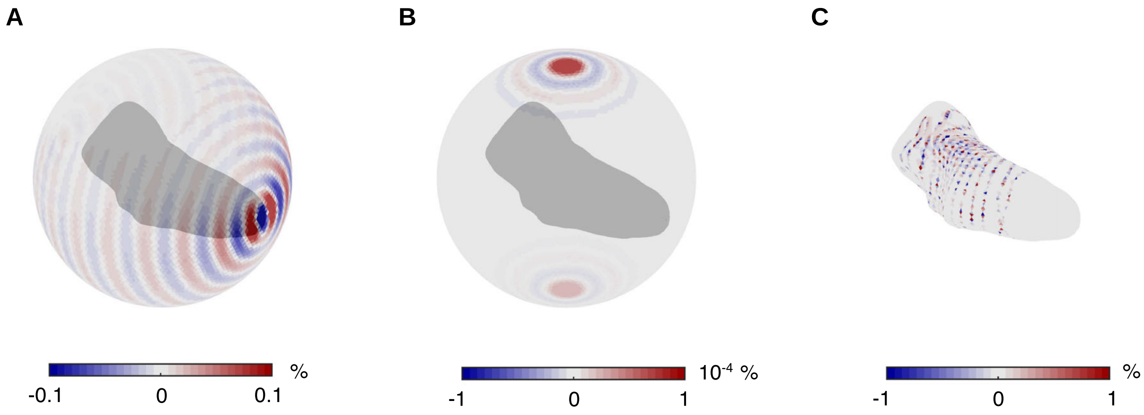

Fig. 12 Numerical uncertainty of the original model for Eros up to degree 20. **A**. Total error, ΔV, on Brillouin sphere. **B**. Impact of coefficient error, $\Delta V^{(\mathrm{CF})}$, on Brillouin sphere. **C**. $\Delta V^{(\mathrm{CF})}/|\Delta V|$ in percentage on body surface

the coefficient errors, which we denote by

$$\begin{bmatrix} \Delta C_{nm} \\ \Delta S_{nm} \end{bmatrix} = \begin{bmatrix} \hat{C}_{nm} \\ \hat{S}_{nm} \end{bmatrix} - \begin{bmatrix} C_{nm} \\ S_{nm} \end{bmatrix}. \tag{A4}$$

Theoretically, the orthogonality ensures $\mathcal{I}_{nm}(V_{pq}) = [C_{pq}\ S_{pq}]\delta_{np}\delta_{mq}$, where δ_{ij} is the Kronecker delta. Numerically, however, the condition cannot be realized to perfection, resulting in $\hat{\delta}_{nn}\hat{\delta}_{mm} \approx 1$ and $\hat{\delta}_{np}\hat{\delta}_{mq} \approx 0$ if $n \neq p$ or $m \neq q$.

To assess the magnitude of $\Delta V^{(\mathrm{CF})}$ we assume that

$$|\Delta V^{(\mathrm{CF})}| \lesssim |\Delta V|, \tag{A5}$$

i.e., the omission errors should not cancel out the effect of the coefficient errors. Then, the impact of the numerical inaccuracy of $\mathcal{I}_{nm}(V_{pq})$ can be quantified by

$$\begin{bmatrix} \Delta \hat{C}_{nm} \\ \Delta \hat{S}_{nm} \end{bmatrix} = \mathcal{I}_{nm}(\Delta V). \tag{A6}$$

Figure 12 shows $\Delta V^{(\mathrm{CF})}$ of the original model in comparison with the total error, ΔV, for Eros. On the Brillouin sphere ΔV consists mostly of omission signals and undulates on the order of 0.01 % of the potential with a maximum of 0.3 % closest to the extremity of the body shape (**A**). $\Delta V^{(\mathrm{CF})}$ varies at the level of 10^{-6} %, i.e., 4 orders of magnitude smaller than ΔV, and is thus negligible. The maximum of 5×10^{-4} % occurs at the poles (**B**). Amplified below the Brillouin sphere in the same way as the coefficients themselves, the coefficient errors account for a part of the total error, which exhibits a strong divergent behavior around the waist (Fig. 6E). Figure 12C shows that the error ratio, $\Delta V^{(\mathrm{CF})}/\Delta V$, is mostly below 1 % over the body surface. The coiled pattern of some scattered, larger values results from the undulation of ΔV whose magnitude diminishes at intervals. Thus, the divergence effect of the model is not due to the contribution of the coefficient errors.

Acknowledgements Hu thanks Dr. Christopher Jekeli for helpful discussions on the convergence behavior of the SHs.

Funding Open Access funding enabled and organized by Projekt DEAL. Funding support is provided by the Emmy Noether-Programm of the German Research Foundation for the project "Geodesy of small bodies: From gravitation to interior structure" (project number: 500329796).

Data Availability Dataset for this study is archived as follows:
Hu, X. (2024). Translated spherical harmonic gravitational field models for Phobos and 433 Eros [Data set]. Zenodo. https://doi.org/10.5281/zenodo.10805461 No software is developed specifically for this work, which is demonstrative and theoretical.

Declarations

Conflict of interest The author has no Conflict of interest to declare that are relevant to the content of this article.

References

Aardoom L (1969) Some transformation properties for the coefficients in a spherical harmonics expansion of the earth's external gravitational potential. Tellus 21(4):572–584

Andert TP, Rosenblatt P, Pätzold M, Häusler B, Dehant V, Tyler GL, Marty JC (2010) Precise mass determination and the nature of Phobos. Geophys Res Lett 37(9):L09202

Beylkin G, Cramer R (2002) Toward multiresolution estimation and efficient representation of gravitational fields. Celest Mech Dyn Astron 84:87–104

Brouwer D, Clemence GM (1961) Methods of celestial mechanics. Academic Press Inc, New York

Bucha B, Sansò F (2021) Gravitational field modelling near irregularly shaped bodies using spherical harmonics: a case study for the asteroid (101955) Bennu. J Geodesy 95(5):56

Casotto S (2000) Translation and rotation of the spherical harmonics coefficients in the expansion of the external potential. In: Astrodynamics Specialist Conference, p 4024

Costin O, Costin RD, Ogle C, Bevis M (2022) On the domain of convergence of spherical harmonic expansions. Commun Math Phys 389(2):875–897

Freeden W (1984) Spherical spline interpolation-basic theory and computational aspects. J Comput Appl Math 11(3):367–375

Garmier R, Barriot J-P (2001) Ellipsoidal harmonic expansions of the gravitational potential: theory and application. Celest Mech Dyn Astron 79(4):235–275

Garmier R, Barriot J-P, Konopliv AS, Yeomans DK (2002) Modeling of the Eros gravity field as an ellipsoidal harmonic expansion from the NEAR Doppler tracking data. Geophys Res Lett 29(8):1231

Giacaglia G (1980) Transformations of spherical harmonics and applications to geodesy and satellite theory. Stud Geophys Geod 24:1–11

Heiskanen WA, Moritz H (1967) Physical Geodesy. W.H Freeman and Company, San Francisco

Hirt C, Kuhn M (2017) Convergence and divergence in spherical harmonic series of the gravitational field generated by high-resolution planetary topography–A case study for the Moon. J Geophys Res (Planets) 122(8):1727–1746

Hobson EW (1931) The theory of spherical and ellipsoidal harmonics (1965 reprint). Chelsea Publishing Company, New York

Hu X (2012) Comparison of ellipsoidal and spherical harmonics for gravitational field modeling of non-spherical bodies. The Ohio State University

Hu X (2016) The exact transformation from spherical harmonic to ellipsoidal harmonic coefficients for gravitational field modeling. Celest Mech Dyn Astron 125(2):195–222

Hu X (2017) Normal gravity fields and equipotential ellipsoids of small objects in the solar system: a closed-form solution in ellipsoidal harmonics up to the second degree. Astrophys J 850(1):107

Hu X, Jekeli C (2015) A numerical comparison of spherical, spheroidal and ellipsoidal harmonic gravitational field models for small non-spherical bodies: examples for the Martian moons. J Geodesy 89(2):159–177

Hu X, Shum CK, Bevis M (2023) A triaxial reference ellipsoid for the Earth. J Geodesy 97(4):29

James RW (1969) Transformation of spherical harmonics under change of reference frame. Geophys J Roy Astron Soc 17(3):305–316

Jeffreys B (1965) Transformation of tesseral harmonics under rotation. Geophys J Int 10(2):141–145

Jekeli C (1981) The downward continuation to the earth's surface of truncated spherical and ellipsoidal harmonic series of the gravity and height anomalies. Air Force Geophysics Laboratory, United States Air Force, Massachusetts

Jekeli C (1983) A numerical study of the divergence of spherical harmonic series of the gravity and height anomalies at the earth's surface. Bulletin Geodesique 57(1–4):10–28

Jones BA, Beylkin G, Born GH, Provence RS (2011) A multiresolution model for small-body gravity estimation. Celest Mech Dyn Astron 111:309–335

Kaula WM (1966) Theory of satellite geodesy. Dover Publications, INC., Mineola, New York

Kholshevnikov C (1977) On convergence of an asymmetrical body potential expansion in spherical harmonics. Celest Mech 16:45–60

Kholshevnikov KV, Shaidulin VS (2015) Existence of a class of irregular bodies with a higher convergence rate of Laplace series for the gravitational potential. Celest Mech Dyn Astron 122:391–403

Klees R, Tenzer R, Prutkin I, Wittwer T (2008) A data-driven approach to local gravity field modelling using spherical radial basis functions. J Geodesy 82(8):457–471

Krarup T (1969) A contribution to the mathematical foundation of physical geodesy. Geod Inst, Copenhagen, p 44

Kusche J, Ilk KH, Rudolph S, Thalhammer M (1998) Application of spherical wavelets for regional gravity field recovery–a comparative study. In: Forsberg R, Feissel M, Dietrich R (eds) Geodesy on the move. Springer, Berlin Heidelberg, pp 213–218

Miller JK, Konopliv AS, Antreasian PG, Bordi JJ, Chesley S, Helfrich CE, Owen WM, Wang TC, Williams BG, Yeomans DK, Scheeres DJ (2002) Determination of shape, gravity, and rotational state of asteroid 433 Eros. Icarus 155(1):3–17

Montenbruck G, Gill E (2000) Satellite orbits. Springer-Verlag, Berlin Heidelberg

Moritz H (1980) Advanced physical geodesy. Abacus Press, Tunbridge Wells Kent

Reimond S, Baur O (2016) Spheroidal and ellipsoidal harmonic expansions of the gravitational potential of small solar system bodies. Case study: Comet 67P/Churyumov-Gerasimenko. J Geophys Res (Planets) 121(3):497–515

Rico JF, López R, Ema I, Ramirez G (2013) Translation of real solid spherical harmonics. Int J Quantum Chem 113(10):1544–1548

Scheeres DJ (2012) Orbital motion in strongly perturbed environments: applications to asteroid, comet and planetary satellite orbiters. Springer, Cham

Schmidt M, Fengler M, Mayer-Gürr T, Eicker A, Kusche J, Sánchez L, Han S-C (2007) Regional gravity modeling in terms of spherical base functions. J Geodesy 81:17–38

Sebera J, Bezděk A, Pešek I, Henych T (2016) Spheroidal models of the exterior gravitational field of Asteroids Bennu and Castalia. Icarus 272:70–79

Sjöberg L (1980) On the convergence problem for the spherical harmonic expansion of the geopotential at the surface of the earth. Bollettino di Geodesia e Scienze Affini 39:261–270

Steinborn EO, Ruedenberg K (1973) Rotation and translation of regular and irregular solid spherical harmonics. Adv Quant Chem 7:1–81

Takahashi Y, Scheeres DJ, Werner RA (2013) Surface gravity fields for asteroids and comets. J Guid Control Dyn 36(2):362–374

Thomas P, Joseph J, Carcich B, Veverka J, Clark B, Bell J III, Byrd A, Chomko R, Robinson M, Murchie S et al (2002) Eros: shape, topography, and slope processes. Icarus 155(1):18–37

Vermeer M (1995) Mass point geopotential modelling using fast spectral techniques; historical overview, toolbox description, numerical experiment. Manuscr Geod 20(5):362–378

Werner RA, Scheeres DJ (1996) Exterior gravitation of a polyhedron derived and compared with harmonic and mascon gravitation representations of asteroid 4769 Castalia. Celest Mech Dyn Astron 65(3):313–344

Wigner EP (1959) Group thoery and its application to the quantum mechanics of atomic spectra. Academic Press Inc, New York

Willner K, Shi X, Oberst J (2014) Phobos' shape and topography models. Planet Space Sci 102:51–59

Winch D, Ivers D, Turner J, Stening R (2005) Geomagnetism and Schmidt quasi-normalization. Geophys J Int 160(2):487–504